communications
physics

ARTICLE

https://doi.org/10.1038/s42005-022-01000-3 OPEN

Non-destructive mapping of stress and strain in soft thin films through sound waves

Guo-Yang Li[1], Artur L. Gower[2], Michel Destrade[3,4]✉ & Seok-Hyun Yun[1]✉

Measuring the in-plane mechanical stress in a taut membrane is challenging, especially if its material parameters are unknown or altered by the stress. Yet being able to measure the stress is of fundamental interest to basic research and practical applications that use soft membranes, from engineering to tissues. Here, we present a robust non-destructive technique to measure directly in-situ stress and strain in soft thin films without the need to calibrate material parameters. Our method relies on measuring the speed of elastic waves propagating in the film. Using optical coherence tomography, we verify our method experimentally for a stretched rubber membrane, a piece of cling film (about 10 μm thick), and the leather skin of a traditional Irish frame drum. We find that our stress predictions are highly accurate and anticipate that our technique could be useful in applications ranging from soft matter devices to biomaterial engineering and medical diagnosis.

---

[1] Harvard Medical School and Wellman Center for Photomedicine, Massachusetts General Hospital, Boston, MA 02114, USA. [2] Department of Mechanical Engineering, University of Sheffield, Sheffield, UK. [3] School of Mathematical and Statistical Sciences, University of Galway, Galway, Ireland. [4] Key Laboratory of Soft Machines and Smart Devices of Zhejiang Province and Department of Engineering Mechanics, Zhejiang University, Hangzhou, PR China. ✉email: michel.destrade@universityofgalway.ie; seok-hyun_yun@hms.harvard.edu

Soft thin films hanging in the air or confined in fluids are found ubiquitously in our daily lives as well as in natural and engineering systems. Examples include cling film packaging food, the eardrum and the diaphragm in our body, and various elastic sheets, membranes, vesicles and bands holding structures together. They are typically under external and/or internal stress, and it is often desirable to know the stress level to understand the environment they are exposed to or interacting with, or to monitor the health of, and changes in, the materials. In general it is challenging to measure non-invasively the stress field in such materials in situ. This is even more difficult if the mechanical properties of the material are unknown and, furthermore, if the original configuration of the material is unknown, which precludes straightforward measurement of strain[1,2].

Various techniques have been devised to measure in-plane stresses[3]. The choice of technique depends on the material type (solid/liquid/type of molecules) and also on the length scale. Essentially all techniques so far rely on the knowledge of the elastic moduli of the material or some specific expected behaviour of the material, which limits application to known or specific materials and structures. For example, in the Langmuir–Blodgett trough[4], a workhorse of membrane biophysics, surface tension is estimated by measuring the amount of force required to insert a Wilhelmy plate into a given membrane. Yet, this force depends on the nature of the surface tension and its accuracy has been questioned for solid-like membranes[5]. Conventional ultrasound methods also require the knowledge of the elastic moduli and acousto-elastic parameters of the materials[6].

In this paper, we describe a technique that allows the stress field to be determined in soft thin films even without a priori knowledge of the material properties or applied strain. The technique uses elastic waves propagating in the film[7,8] followed by a simple algorithm to determine the stress from their measured wave speeds. Wave speeds change with stress, just like the sound of a guitar changes when strings are tightened. From the measured wave speeds at several frequencies we show how to recover the in-plane stress and strain in stretched rubber membrane, cling film, and animal skin directly, without knowing nor needing any physical parameters other than mass density and current thickness. For ultra-thin sheets such as cling film, the current thickness is hard to measure accurately, but we show that it is not needed for the estimation of the stress. Here, we use optical coherence tomography (OCT) to visualise the elastic waves and measure their speeds in an audible frequency range. This range (1–20 kHz) is well suited for soft materials with thickness ranging from sub-micron to a few hundreds of micrometers.

Results

Figure 1 summarises the main findings. Fig. 1c–e show the wavefronts generated by a vibrating spherical probe hitting a thin rubber membrane (Fig. 1a, b) with frequency $f = 6$ kHz, as recorded by OCT imaging in the unstressed ($N = 0$) and fully stressed states ($N = 6$ weights of 20 g each added to pull on the sheet, creating a stress of $\sigma_1 = 200$ kPa, see Methods). While in the unstressed state the wave propagates at the same speed in all directions (circular wavefronts), the application of stress clearly induces anisotropy for the wave speed (elliptical wavefronts with the major axis aligned with x_1, i.e., the direction of the uniaxial tension), leading to a significant increase of the speed along the uniaxial tension, and a decrease along the perpendicular direction (see Supplementary Note 8). This observation is confirmed when solving the dispersion relation (see Methods) of the A0 fundamental antisymmetric propagation mode for different levels of stress ($N = 0, \dots 6$) as shown in Fig. 1f. From our experimentally measured phase wave speeds we then deduce by linear least squares regressions the values of α and γ, the two quantities required to determine stress and strain (see Methods and Supplementary Note 7).

Figure 1g shows the resulting Cauchy stress (i.e., $\sigma_1 = \alpha - \gamma$) and how it compares with that actually applied to the film, with errors around 5%. Similarly, we measure σ_2 using the wave speeds along x_2, also shown in Fig. 1g. As the uniaxial tension is applied along x_1 only, σ_2 is expected to be close to zero, which is what the experiments confirm.

According to our analysis (Eq. 2 in Methods), the extension stretch is $\lambda_1 = (\alpha/\gamma)^{1/3}$ in uni-axial deformation. Figure 1h shows the identified stretch ratio (i.e., $(\alpha/\gamma)^{1/3}$, as computed from the speed measurements) and the comparison with the experimental λ_1. We measured the latter directly by tracking the deformation of a grid drawn on the membrane, and we also computed it from the thickness variation as $\lambda_1 = (h_0/h)^2$. Again an excellent agreement is achieved, with a maximum error of ~3%. Similarly, we applied the method along the x_2 axis to obtain λ_2; in the uni-axial tension of an incompressible, initially isotropic solid, it is expected to behave as $\lambda_1^{-1/2}$, as we indeed verified.

Finally, Fig. 1i shows the agreement between the stress found from the speed measurements as a function of the identified stretch with the data obtained by an independent (destructive) tensile test and thus validates further the proposed method.

Next we measured the stress in stretched plastic wrap, a.k.a. cling film (Fig. 2a) made of polyethylene. The typical thickness of cling film ranges from 8 to 13 µm, which is beyond the capabilities of accurate axial resolution in OCT. Nonetheless, we can still generate and study Lamb wave propagation in the stretched cling film with the OCT system. Here, we were able to evaluate the stress in the cling film (but not the strain): we proved (see Methods) that $\sigma_1 = \alpha - \gamma = \rho v^2$ for ultra-thin stretched films, almost independently of frequency. Figure 2b shows the data of wave dispersion for the unstressed and fully stressed states, obtained with a similar set-up. In Fig. 2c, we report the stress identified by this method, which shows very good agreement with the values of the stress actually applied (maximum error ~ 11%).

Finally we applied our technique to measure the stress in the drumhead of a musical instrument called the bodhrán drum, a traditional Irish drum made with goat skin. The thickness of the skin was measured to be 360 ± 30 µm. We performed in situ measurements on the drumhead (Fig. 3a) at normal (dry) and hydrated conditions of the skin. In the dry condition, the fundamental resonance frequency of the instrument was ~84 Hz, and it was decreased to ~36 Hz after hydration (see Supplementary Note 10). The goat skin is intrinsically anisotropic, but our experiments revealed almost circular wave profiles (Supplementary Movies 3 and 4). This is well explained by the large radial stress in the drum, which stretches collagen fibres along the stress field[9]. The applied strain is transversely isotropic (equi-biaxial in the radial/circumferential directions) and thus, for all intends and purposes, acoustic wave propagation is isotropic in the drum plane. Figure 3b shows the dispersion relations of the skin in the dry and damp states, obtained at a region in the drum head. We determined from the experimental data that the amount of radial stretch in the dry skin is 0.28% and that humidification relaxed it to 0.20% (Fig. 3c). The corresponding stress is changed from 3.79 MPa (dry) to 1.31 MPa (damp). Noting that the strain is small, with the stress and strain we can derive the Young modulus of the skin to be ~680 MPa for dry skin and ~330 MPa for the damp skin, which shows that humidification not only decreases significantly the stretch but also the stiffness of the skin.

The result reveals how much the humidification changed the stiffness and the tension of the skin. Hydration alters the

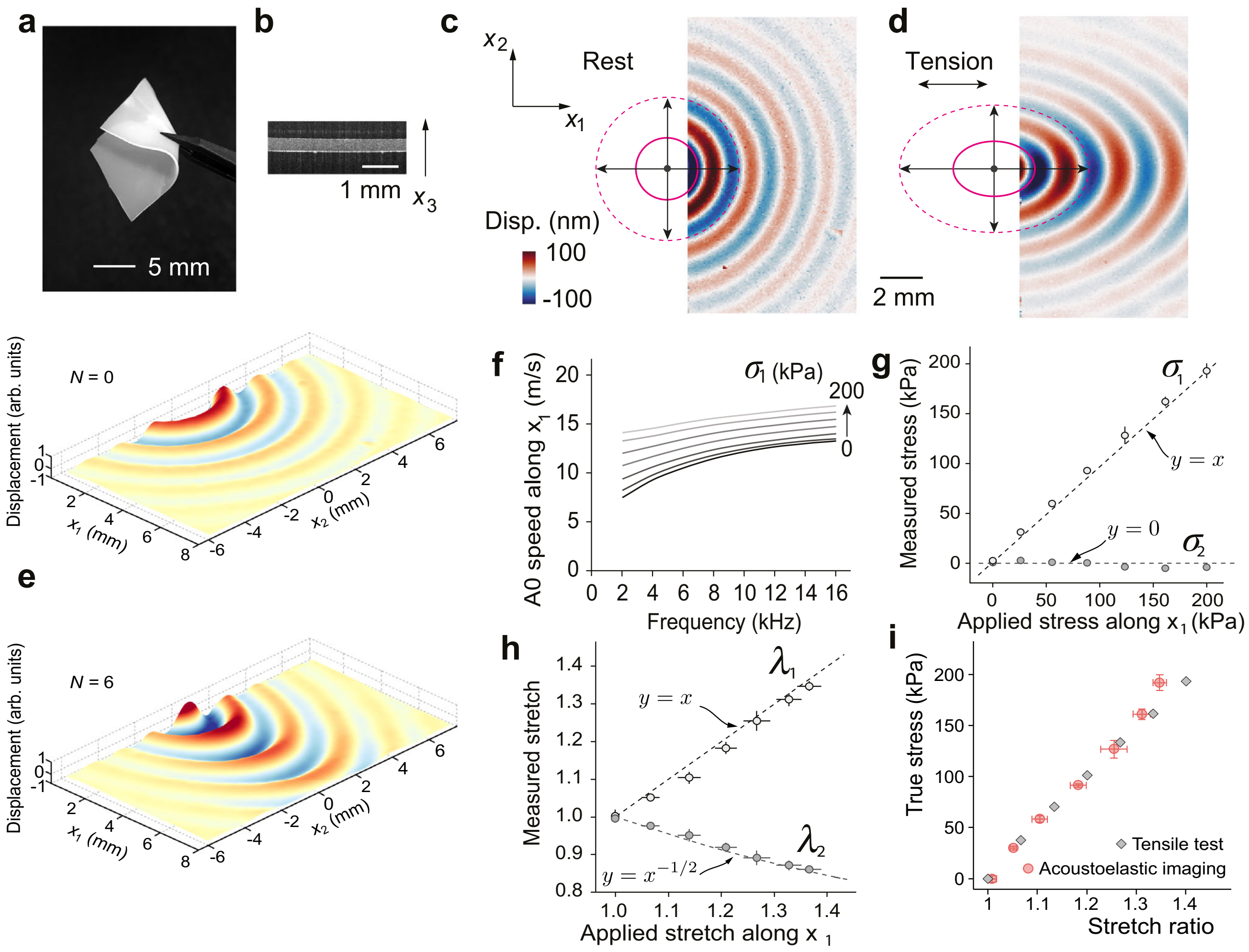

Fig. 1 Imaging and analysing elastic waves in a stretched rubber membrane. **a** Photograph of our rubber sheet. **b** Optical Coherence Tomography (OCT) cross-sectional image. **c**, **d** Wave profiles measured by OCT when the film is **c** stress-free and **d** subject to uniaxial stress $\sigma_1 \simeq 200$ kPa, see Supplementary Movies 1 and 2. The wavefronts become elliptical when stretched. **e** Corresponding 3D wavefronts, obtained by measuring the vertical displacement from the phase change in the interference signal of the OCT; N indicates the number of weights (each with mass 20 g). **f** Dispersion relations of the A0 mode obtained at different levels of stress. Each curve is an average over six measurements (for clarity the error bar is not shown here but can be found in Supplementary Fig. 11). **g** Comparison between measured and applied stress values (σ_1, σ_2: stress components along, and perpendicular to, the direction of tension, respectively). For reference, the dashed lines show where the measured stresses are equal to the applied stresses. **h** Comparison between the measured and applied stretch values (λ_1, λ_2: stretch ratios along, and perpendicular to, the direction of tension, respectively). Dashed lines, expected 1 and -1/2 power laws of the stretches for reference. **i** Stress-strain curve from the measured data compared to that measured by a standard tensile test. Error bars are the standard deviations from six measurements.

resonance frequency (pitch) of the instrument, which is proportional to $\sqrt{\sigma_1/\rho}$. The 65% reduction in tension predicts about 46% decrease in resonance frequency. This is comparable to the measured 57% decrease for the resonance frequency (from 84 Hz to 36 Hz). The discrepancy is mostly likely due to a change in the mass density as well as to the spatially nonuniform hydration applied across the large drumhead (41 cm diameter).

Discussion

We proposed a method to evaluate directly the in-plane stress and strain present in a taut film or membrane. The method is nearly model-free, in the sense that it is independent of, and does not require, the material's elastic constants. The method only required the mass density and film thickness.

We validated our method experimentally and found a high level of accuracy for the measured stress and strain in a thin rubber film (0.5 mm thickness). We went on to apply the same method to an ultra-thin membrane of stretched cling film (12 µm thickness). In that case we were able to determine the stress accurately, even though theoretically, our method was designed for incompressible materials. Cling film is compressible, with initial Poisson's ratio $\nu \simeq 0.32$ and also exhibits significant plasticity. In Supplementary Note 3, we show that extending the method to accommodate compressibility only adds a small error in the low frequency regime, which helps explain the success of the method here. We also managed to estimate the in situ, unknown, amounts of stress and stretch in the skin of a bodhrán, and found that humidifying it decreased the stretch by almost 30% and the stress by 65%. In that analysis we did not consider whether the mass density was changed by humidification, so that our results are approximate.

Our method applies primarily to elastic materials, and also to weakly viscoelastic materials because there is evidence that viscosity does not affect the wave speeds significantly, only their amplitude, provided the attenuation length is much larger than

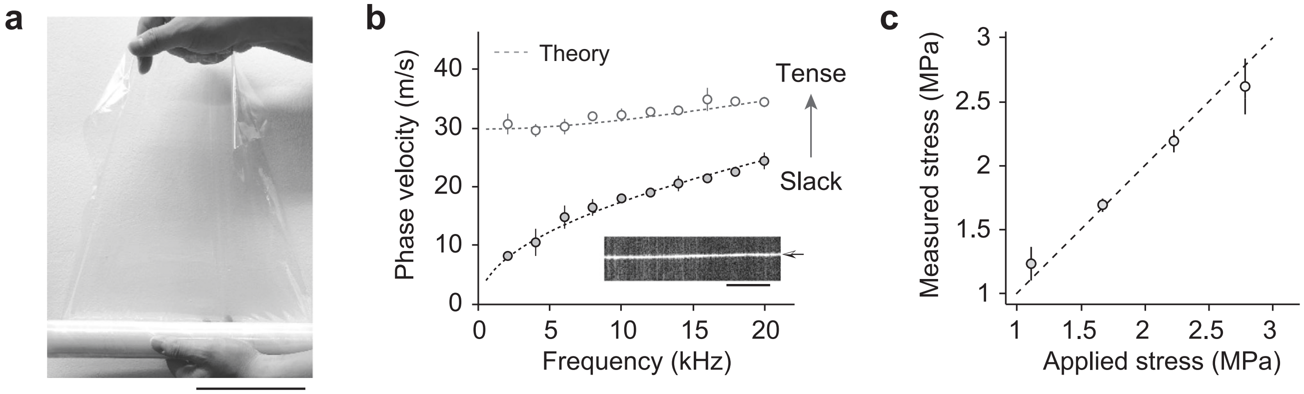

Fig. 2 Measuring the stress in cling film. a Photograph of the cling film. Scale bar, 10 cm. **b** Dispersion curves for a cling film, in the stress-free (lower) and stressed (upper) states. Markers, experiment. Curves, theory. Inset, Optical Coherence Tomography (OCT) transverse image of the cling film, which is too thin for an accurate thickness measurement by OCT. Scale bar, 0.5 mm. **c** Comparison between the applied and identified stress. Dashed line, 45° line for reference. Error bars are the standard deviations from five measurements.

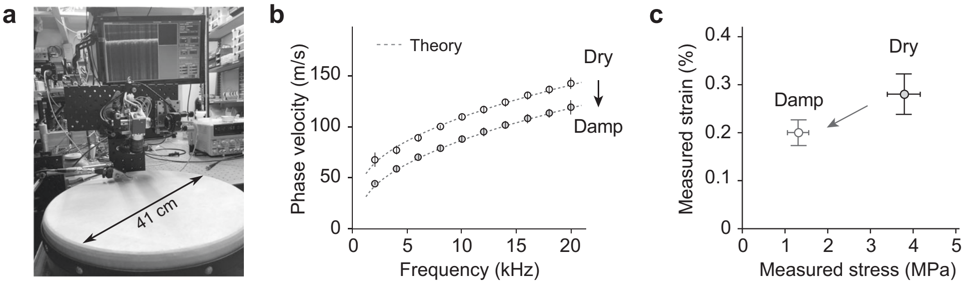

Fig. 3 Measuring the stress in a drum head. a Photograph of the experimental set up. A real-time Optical Coherence Tomography image is displayed in the monitor. **b** Dispersion relations measured in the dry (upper) and damp (lower) states. Markers, experiment. Dashed curves, theory. **c** Stresses and strains measured in the dry and damp states. Error bars are the standard deviations over five measurements.

the wavelength[10]. Furthermore, for thin plates, only low frequency waves are needed to estimate the stress, in which case viscosity has a very small effect on the wave speed. However, larger frequencies, or highly viscous materials, call for more involved modelling with parameters including viscosity[11,12].

Many real-life materials such as composites or biomaterials possess intrinsic anisotropy. Accounting for preferred directions complicates the equations of acousto-elasticity greatly, and leads to a breakdown of the proposed method, except maybe in special cases, such as for example for waves propagating along fibers when they are aligned with the principal directions of pre-stretch, see the recent advances in that direction[13,14].

It is relatively straightforward to extend our method to thin structures in contact with fluids or (isotropic) gel-like matters, either on one or both sides, such as the dura mater enveloping the brain (after craniotomy)[15] and the cornea[16] as well as blood vessel walls[17]. Our work is expected to pave the way to practical applications.

Methods

Theory. Consider a stretched film with the coordinate axes (x_1, x_2, x_3) aligned with its edges, where $-h \leq x_3 \leq h$, so that the film has thickness $2h$, see Fig. 4a. To determine the stress, we consider the speed of elastic waves travelling along the x_1 direction of a free film, with no displacement in the x_2 direction, and polarised in the (x_1, x_3) plane. These are the so-called Lamb waves.

The dispersion relation, relating the wave speed v to the wavenumber k, for the anti-symmetric (flexural, exponent $+1$) and symmetric (extensional, exponent -1) modes is[18]

$$4\sqrt{\frac{\alpha-\rho v^2}{\gamma}}\left(\frac{\tanh\sqrt{\frac{\alpha-\rho v^2}{\gamma}}kh}{\tanh kh}\right)^{\pm 1} = \left(1+\frac{\alpha-\rho v^2}{\gamma}\right)^2, \tag{1}$$

where α and γ are instantaneous elastic moduli. Determining them gives direct access to the state of in-plane stress and strain, because

$$\alpha-\gamma=\sigma_1, \qquad \alpha/\gamma=\lambda_1^3, \tag{2}$$

see Supplementary Note 1 for details.

This dispersion equation assumes the membrane is incompressible, isotropic when there is no stress, and is subjected to moderate strains. These assumptions are an excellent approximation for most rubber-like materials and lead to the third-order incompressible elastic strain energy[19], which depend on only two material constants: the initial shear modulus μ ($\mu = E/3$, where E is the Young modulus), and the third-order Landau constant A (also known as n in the expansion of Murnaghan[20,21]).

The dispersion relation Eq. 1 yields multiple solutions for the speed v at a given frequency (or wavenumber k). The waves with the smallest speeds, called the fundamental modes A0 and S0, are the easiest to measure. The principle of our method is to extract the moduli α and γ from the A0 and S0 modes, as we detail below, and determine the stress and stretch using Eq. 2. Figure 4b shows how these modes are sensitive to stress from a uni-axial extension of 5% (full lines) to 10% (dashed lines), for a specific choice of (ρ, μ, A).

For a very thin film, or small k, we can take $kh \to 0$ in Eq. 1 to obtain $\rho v^2 = \alpha - \gamma$ or $\alpha + 3\gamma$ for the A_0 or S_0 modes, respectively. On the other hand, for a very thick film, or large k, we can take $kh \to \infty$ to obtain $\rho v^2 = \alpha - \eta_0^2\gamma$ where $\eta_0 = 0.2956$ is the real root of the cubic $x^3 + x^2 + 3x - 1 = 0$ (Rayleigh surface wave limit). In principle, if two of these three limiting wave speeds can be measured, then α and γ, and thus the stress and stretch can be determined through Eq. 2. In fact, the first limit gives the stress directly according to Eq. 2 (later we show how this remark leads to an accurate stress measurement in an ultra-thin film such as cling film.).

In practice, it might prove difficult to attain reliable values for these limits in general, especially the third one (as a thin film is the opposite of a half-space, where a Rayleigh wave propagates). It is also impractical to use templates such as Fig. 4a for other values of the speeds, because the graphs are very sensitive[22] to the $\{\mu, A, \lambda_1\}$ values (hence two very different sets could yield very close plots).

Instead, we rely on a master graph, independent of the material and physical parameters $\rho, \mu, A, \sigma_1, \lambda_1$. For the A0 mode we define $\eta_{A0} = \sqrt{(\alpha-\rho v^2)/\gamma}$, and the corresponding dispersion equation is

$$4\,\eta_{A0} \tanh \eta_{A0}kh \coth kh = \left(1+\eta_{A0}^2\right)^2. \tag{3}$$

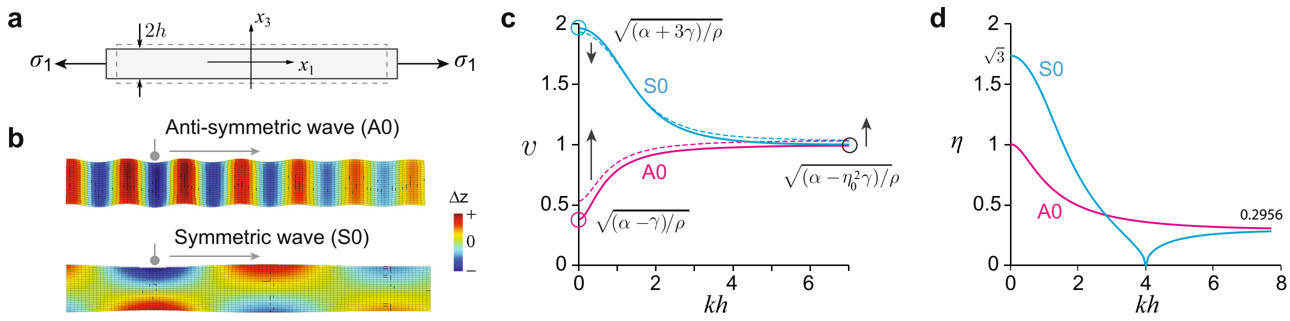

Fig. 4 Acousto-elastic effect for Lamb waves. a A thin plate with thickness $2h$ put under tensile stress σ_1 along x_1. **b** Modal shapes of the fundamental anti-symmetric (A0) and symmetric (S0) Lamb waves, with color-coded vertical displacement Δz. **c** Dispersion curves (kh Vs v where k is the wavenumber and v is the wave speed) for the A0 and S0 modes in a hypothetical incompressible material with initial shear modulus $\mu = 1.0$ kPa, Landau third-order modulus $A = -6.4$ kPa and mass density $\rho = 1.0$ g/cm^3, subject to a uni-axial extension of 5% (stretch $\lambda_1 = 1.05$, full lines) and then 10% ($\lambda_1 = 1.10$, dashed lines). The circles indicate three asymptotic values of the dispersion curves, and arrows indicate their direction of change with tension (α and γ are instantaneous elastic moduli, $\eta_0 = 0.2956$). **d** Master curves for the dispersion relation of all materials and pre-stresses/stretches (independent of ρ, μ, A, σ_1, λ_1): identifying two values of η, the dimensionless variable on the vertical axis, from measurements gives access to the stress and the strain.

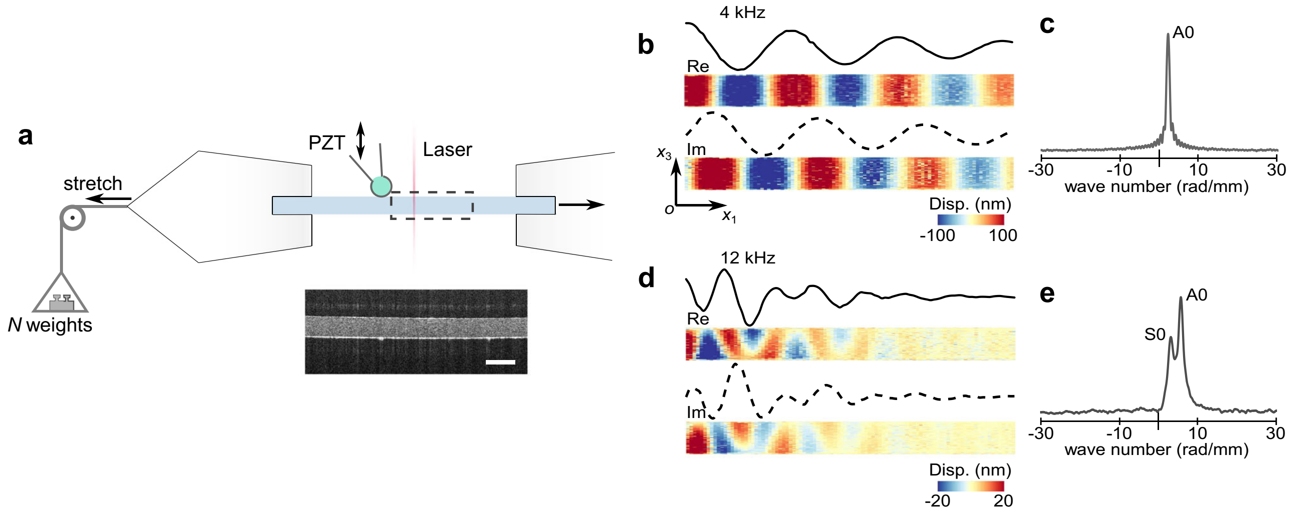

Fig. 5 Measuring the speed of Lamb waves in a stretched rubber thin film with Optical Coherence Tomography (OCT). a Schematic of the experimental setup. The OCT operates synchronously with the piezoelectric transducer (PZT) probe to perform an motion-brightness (M-B) scan. Inset, OCT transverse image of the film (scale bar, 2 mm). **b** Real and imaginary parts of the displacement field when the stimulus frequency is 4 kHz. The curves show the displacements extracted from the upper surface of the sample. **c**, Wavenumber domain data obtained by Fourier transform of the spatial domain data. A peak corresponding to the A0 mode can be clearly identified from this curve. **d**, **e** Spatial and wavenumber domain data obtained at 12 kHz. Two peaks, corresponding to the A0 and S0 modes, can be identified from the wavenumber domain data.

For the S0 mode, we define $\eta_{S0} = \sqrt{(\rho v^2 - \alpha)/\gamma}$ and get

$$4\eta_{S0}\cot\eta_{S0}kh\tanh kh = \left(1-\eta_{S0}^2\right)^2, \tag{4}$$

see Fig. 4c for the resulting $\eta - kh$ master curves (and Supplementary Note 1). Then we obtain α and γ from these master curves by placing two points on the curves from speed/frequency measurements, which leads to a system of two equations. In practice, we may increase the accuracy by making more than two measurements and optimising for α, γ by linear least squares regression (Supplementary Note 7).

For ultra-thin films such as cling film (less than 13 μm thick), the OCT system is not able to measure the thickness accurately, but it can image waves and measure their speed. Take for example the 2 kHz measurement for the stressed cling film, see Fig. 2b: there, $v \simeq 32$ m.s^{-1} and $2h < 13$ μm, which means that $kh < 2.73 \times 10^{-3}$. Thus, solving Eq. 3 we find that $0.99995 < \eta_{A0}^2 < 1.0$, so that for all intents and purposes, $\eta_{A0}^2 = (\alpha - \rho v^2)/\gamma = 1$. It follows that at that frequency, the stress $\sigma_1 = \alpha - \gamma$ is found directly as $\sigma_1 = \rho v^2$.

Experimental setup. We devised the experimental setup shown in Fig. 5a and Supplementary Fig. 10, based on a home-built, swept-source optical coherence tomography (OCT) system[16]. This system has an A-line rate of 43.2 kHz, axial resolution of ~15 μm and transverse resolution of ~30 μm, using a polygon swept laser with a tuning range of 80 nm and a center wavelength of 1280 nm. The optical beam is scanned using a two-axis galvanometer scanner. To excite Lamb waves in the film we used a probe driven by a vibrating piezoelectric transducer (Thorlabs, PA4CEW). The plastic probe was 3D-printed and has a spherical tip with a 2 mm diameter. A small force (~20 mN) was applied to the probe to keep it in contact with the sample. The optical beam scan was synchronised with the probe vibration to operate in an motion-brightness (M-B) scan mode, to capture the wave propagating along the direction of tension (x_1), and then along x_2. The frequency of the vibration was step-tuned from 2 to 20 kHz with an interval of 2 kHz. At each frequency, we acquired the amplitudes and phases of the vibrations at 96 transverse locations (see Supplementary Note 4 for details of the M-B scan). To demonstrate the stress-induced anisotropy visually, we also scanned the laser beam along the out-of-plane direction (x_3) to obtain a top view of the wave propagation within the film, see Fig. 1c, d. The vertical displacement near the probe contact point at the sample was in the order of 100 nm in the frequency range. To measure this small vibration, we used the phase change in the interference signal of the OCT[16], see Fig. 1e.

Figure 5b, d shows the real and imaginary parts of the vertical displacements obtained at 4 kHz and 12 kHz, respectively, when two weights are used to load the rubber membrane. The curve above each map shows the displacement extracted from the upper surface of the membrane.

To measure the wavenumber k, and thus the wave speed $v = 2\pi f/k$ for a given frequency, the surface displacement was Fourier-transformed from the spatial domain to the wavenumber domain, as shown in Fig. 5c, e. The standard deviation error in the wavenumber measurement is estimated to be about 0.1% (see Supplementary Note 5). At 4 kHz, the A0 mode is predominantly excited so that only one peak can be identified in the wavenumber domain. At 12 kHz, another peak that corresponds to the S0 mode emerges at a lower wavenumber besides the A0 mode (see also Supplementary Note 6). The wavenumbers of the A0 mode obtained from Fig. 5c, e are 2.43, 5.46rad.mm^{-1}, respectively. Taking the film thickness and the wavenumbers together, we get $2kh \simeq 1.14$ at 4 kHz and $2kh \simeq 2.56$ at 12 kHz, showing that these measurements are taken in the low frequency regime. Our sensitivity analysis (see Supplementary Note 2) suggests that measurements in the low frequency regime give a better detection sensitivity for the mechanical stress. We used the data of A0 for the subsequent analysis since it is the dominant mode in the frequency range studied here.

For the experiments on the rubber sheet and cling film, the sample was clamped along its two short edges and one clamp was pulled horizontally by a cord connected to $N = 1$ to 6 weights ($m = 20$ g each) to apply a uniaxial tension σ_1 with increasing magnitude, as shown in Fig. 5a. It was measured as $\sigma_1 = \lambda_1 Nmg/(2W_0h_0)$, where $g = 9.8$m.s^{-2} is the acceleration of gravity. We took the average of results obtained from the loading and unloading protocols to minimise the effect of hysteresis.

Each time a new weight ($N = 0, 1, \ldots, 6$) was added, the current film thickness $2h$ was measured by the OCT image, from which the stretch ratio $\lambda_1 = \lambda_3^{-2} = (h_0/h)^2$ was evaluated (assuming a uniaxial deformation took place), see Supplementary Fig. 12. The measured stretch ratio agreed well with that obtained by the deformation of the grids drew on the surface of the rubber film. The stretch ratio of the film reached $\lambda_1 \simeq 1.37$ (37% extension) when $N = 6$.

Materials. The rubber sheet had mass density $\rho \simeq 1,070$kg.m^{-3} and refractive index $n \simeq 1.4$. The initial dimensions were $2h_0 \simeq 0.5$ mm, $W_0 = 16$ mm, $L_0 = 40$ mm, large enough to avoid wave reflections at the edges (see Fig. S4 for photos of the sample and the experimental setup). The membrane was prepared from the Ecoflex 00–50 material (Smooth-On Inc), by mixing the Ecoflex rubbers 1A and 1B to 1:1 ratio by weight. The mixture was poured into a mould and cured at room temperature overnight. Then the sample was post-cured in an oven at 80 °C for 2 h. To characterise its mechanical properties, we cut a small piece ($0.5 \times 5 \times 18$ mm^3) from the sample and performed a tensile test with a uniaxial tensile testing machine (eXpert 4000 Micro Tester, Admet, Norwood, USA). By curve fitting we found that the initial shear modulus was $\mu \simeq 180$ kPa and the Landau constant was $A \simeq -1.3$ MPa (see Supplementary Note 9). These material parameters were then used to plot the theoretical dispersion curves, although ultimately they are not needed.

We used a common household cling film (plastic wrap) made of 100% polyethylene, with mass density $\rho \simeq 930$ kg.m^{-3}. The typical thickness of cling film ranges from 8 to 13 μm. Here, we used Brillouin microscopy[23] to accurately measure the initial thickness of the film, which was $2h_0 = 11.7 \pm 0.3$ μm. This is close to the axial resolution of the OCT system, and so we could not track h with the deformation.

The bodhrán was purchased from Hobgoblin Music, MN, USA. The OCT measurement was performed on the intact instrument. On separate direct measurements after removing the skin from the frame, we found $h_0 = 0.36 \pm 0.03$ mm and $\rho = 831 \pm 65$kg.m^{-3}, respectively. To characterise the fundamental vibration frequencies of the dry and damp bodhrán, the centre of the drumhead was beaten every 10 s and the sound was recorded with a cellphone 10 cm away from the drumhead, using the Google Science Journal App (see Supplementary Note 10).

Data availability

The data that support the findings of this study are available from the authors on reasonable request.

Code availability

The code to get the master graph from the dispersion equation was prepared with Matlab R2021a, which is available from the authors on reasonable request.

Received: 31 January 2022; Accepted: 24 August 2022;
Published online: 17 September 2022

References

1. Gómez-González, M., Latorre, E., Arroyo, M. & Trepat, X. Measuring mechanical stress in living tissues. *Nat. Rev. Phys.* **2**, 300–317 (2020).
2. Schajer, G. S. Advances in hole-drilling residual stress measurements. *Exp. Mech.* **50**, 159–168 (2009).
3. Butt, H.-J., Graf, K. & Kappl, M. Physics and chemistry of interfaces (John Wiley & Sons, 2013).
4. Erbil, H. Y. et al. Surface chemistry of solid and liquid interfaces (Blackwell, 2006).
5. Aumaitre, E., Vella, D. & Cicuta, P. On the measurement of the surface pressure in Langmuir films with finite shear elasticity. *Soft Matter* **7**, 2530–2537 (2011).
6. Shi, F., Michaels, J. E. & Lee, S. J. In situ estimation of applied biaxial loads with Lamb waves. *J. Acoustical Soc. Am.* **133**, 677 (2013).
7. Lanoy, M., Lemoult, F., Eddi, A. & Prada, C. Dirac cones and chiral selection of elastic waves in a soft strip. *Proc. Natl Acad. Sci.* **117**, 30186–30190 (2020).
8. Thelen, M., Bochud, N., Brinker, M., Prada, C. & Huber, P. Laser-excited elastic guided waves reveal the complex mechanics of nanoporous silicon. *Nat. Commun.* **12**, 1–10 (2021).
9. Deroy, C., Destrade, M., Mc Alinden, A. & Ní Annaidh, A. Non-invasive evaluation of skin tension lines with elastic waves. *Ski. Res. Technol.* **23**, 326–335 (2017).
10. Bercoff, J., Tanter, M., Muller, M. & Fink, M. The role of viscosity in the impulse diffraction field of elastic waves induced by the acoustic radiation force. *IEEE Trans. Ultrason., Ferroelectr., Frequency Control* **51**, 1523–1536 (2004).
11. Berjamin, H., Destrade, M. & Parnell, W. On the thermodynamic consistency of Quasi-linear viscoelastic models for soft solids. *Mech. Res. Commun.* **111**, 103648 (2021).
12. Rooij, R. & Kuhl, E. Constitutive modeling of brain tissue: current perspectives. *Appl. Mech. Rev.* **68**, 010801 (2016).
13. Remeniéras, J. P. et al. Acousto-elasticity of transversely isotropic incompressible soft tissues: Characterization of skeletal striated muscle. *Phys. Med. Biol.* **66**, 145009 (2021).
14. Bied, M. & Gennisson, J. L. Acoustoelasticity in transversely isotropic soft tissues: Quantification of muscle nonlinear elasticity. *J. Acoustical Soc. Am.* **150**, 4489–4500 (2021).
15. Hartmann, K., Stein, K. P., Neyazi, B. & Sandalcioglu, I. E. Optical coherence tomography of cranial dura mater: Microstructural visualization in vivo. *Clin. Neurol. Neurosurg.* **200**, 106370 (2021).
16. Ramier, A., Tavakol, B. & Yun, S.-H. Measuring mechanical wave speed, dispersion, and viscoelastic modulus of the cornea using optical coherence elastography. *Opt. Express* **27**, 16635–16649 (2019).
17. Li, G.-Y. et al. Guided waves in pre-stressed hyperelastic plates and tubes: Application to the ultrasound elastography of thin-walled soft materials. *J. Mech. Phys. Solids* **102**, 67–79 (2017).
18. Rogerson, G. & Fu, Y. An asymptotic analysis of the dispersion relation of a pre-stressed incompressible elastic plate. *Acta. Mechanica* **111**, 59–74 (1995).
19. Destrade, M., Gilchrist, M. D. & Saccomandi, G. Third-and fourth-order constants of incompressible soft solids and the acousto-elastic effect. *J. Acoustical Soc. Am.* **127**, 2759–2763 (2010).
20. Murnaghan, F. D. Finite deformation of an elastic solid (Wiley, 1951).
21. Hughes, D. S. & Kelly, J. L. Second-order elastic deformation of solids. *Phys. Rev.* **92**, 1145–1149 (1953).
22. Gandhi, N., Michaels, J. E. & Lee, S. J. Acoustoelastic Lamb wave propagation in biaxially stressed plates. *J. Acoustical Soc. Am.* **132**, 1284–1293 (2012).
23. Scarcelli, G. et al. Noncontact three-dimensional mapping of intracellular hydromechanical properties by Brillouin microscopy. *Nat. Methods* **12**, 1132–1134 (2015).

Acknowledgements

This study was supported by grants P41-EB015903, R01-EY027653, DP1-EB024242 from the National Institutes of Health (USA) for G.Y.L and S.H.Y; by the 111 Project for International Collaboration No. B21034 (Chinese Government, PR China), by the Seagull Program (Zhejiang Province, PR China), by the National Natural Science Foundation of China (No. 11872329), by the Natural Science Foundation of Zhejiang Province (No. LD21A020001), and by a travel grant from the UK Acoustic Network funded by the EPSRC (EP/R005001/1) for M.D.; by the Shift2Rail grant from the European Commission - Horizon 2020, and by the EPSRC (EP/V012436/1) for A.L.G. For the purpose of Open Access, the authors have applied a Creative Commons Attribution (CC BY) licence to any Author Accepted Manuscript version arising. The authors thank Amira Eltony and Xu Feng for help with the measurements, and Pasquale Ciarletta, Niall Colgan and Giuseppe Zurlo for valuable feedback.

Author contributions

G.Y.L., A.G., and M.D. conceived the study. G.Y.L., A.G., and M.D. developed the theoretical model. G.Y.L. conducted the experiments. G.Y.L. and S.H.Y. analysed the results. All authors wrote, reviewed and revised the manuscript.

Competing interests

The authors declare no competing interests.

Additional information

Supplementary information The online version contains supplementary material available at https://doi.org/10.1038/s42005-022-01000-3.

Correspondence and requests for materials should be addressed to Michel Destrade or Seok-Hyun Yun.

Peer review information *Communications Physics* thanks Anthony Mulholland and the other, anonymous, reviewer(s) for their contribution to the peer review of this work.

Reprints and permission information is available at http://www.nature.com/reprints

Supplementary Materials
for
Non-destructive mapping of stress and strain in soft thin films through sound waves

Guo-Yang Li
Harvard Medical School and Wellman Center for Photomedicine,
Massachusetts General Hospital, Boston, MA 02114, United States.

Artur L Gower
Department of Mechanical Engineering, University of Sheffield, Sheffield, United Kingdom

Michel Destrade
School of Mathematical and Statistical Sciences, NUI Galway, Galway, Ireland;
Key Laboratory of Soft Machines and Smart Devices of Zhejiang Province and
Department of Engineering Mechanics, Zhejiang University, Hangzhou, PR China

Seok-Hyun Yun
Harvard Medical School and Wellman Center for Photomedicine,
Massachusetts General Hospital, Boston, MA, USA

SUPPLEMENTARY NOTE 1: LAMB WAVES IN A STRESSED FILM

Consider a plate with edges parallel to the Cartesian coordinates (x_1, x_2, x_3), where $-h \leq x_3 \leq h$ so that the plate's current thickness is $2h$, as illustrated in Supplementary Figure 1(a). Aligned with this axes are the principal stress σ_1, σ_2, σ_3, and we assume the faces are stress free, so that $\sigma_3 = 0$.

The motion of a Lamb wave travelling along x_1 axis with speed v and wavenumber k in an elastic incompressible plate is in general governed by the following dispersion equation [1],

$$\left(\frac{\tanh s_1 kh}{\tanh s_2 kh}\right)^{\pm 1} = \frac{s_2(s_1^2+1)^2}{s_1(s_2^2+1))^2}, \tag{S.1}$$

for symmetric (+1 exponent) and anti-symmetric modes (-1 exponent), and where s_1^2, s_2^2 are the roots of the quadratic

$$\gamma s^4 - (2\beta - \rho v^2)s^2 + \alpha - \rho v^2 = 0. \tag{S.2}$$

Here α, β and γ are instantaneous elastic moduli, which satisfy

$$\alpha - \gamma = \sigma_1, \qquad \alpha/\gamma = \lambda_1^2/\lambda_3^2, \tag{S.3}$$

independent of the materials properties. When the stress are due to an elastic deformation with the pre-stretches λ_1, λ_2, λ_3 along (x_1, x_2, x_3), such that $\lambda_1\lambda_2\lambda_3 = 1$ because of incompressibility, then

$$\alpha = \frac{\sigma_1 - \sigma_3}{\lambda_1^2 - \lambda_3^2}\lambda_1^2, \qquad \gamma = \frac{\sigma_1 - \sigma_3}{\lambda_1^2 - \lambda_3^2}\lambda_3^2, \qquad 2\beta = \lambda_1^2\frac{\partial^2 W}{\partial \lambda_1^2} - 2\lambda_1\lambda_3\frac{\partial^2 W}{\partial\lambda_1\partial\lambda_3} + \lambda_3^2\frac{\partial^2 W}{\partial\lambda_3^2} + 2\lambda_1\lambda_3\frac{\lambda_1\frac{\partial W}{\partial\lambda_3} - \lambda_3\frac{\partial W}{\partial\lambda_1}}{\lambda_1^2 - \lambda_3^2}, \tag{S.4}$$

where $W = W(\lambda_1\lambda_2\lambda_3)$ is the strain energy density, and the identities (S.3) follow immediately. Note that they also hold when the origin of the pre-stress is not known [2, 3].

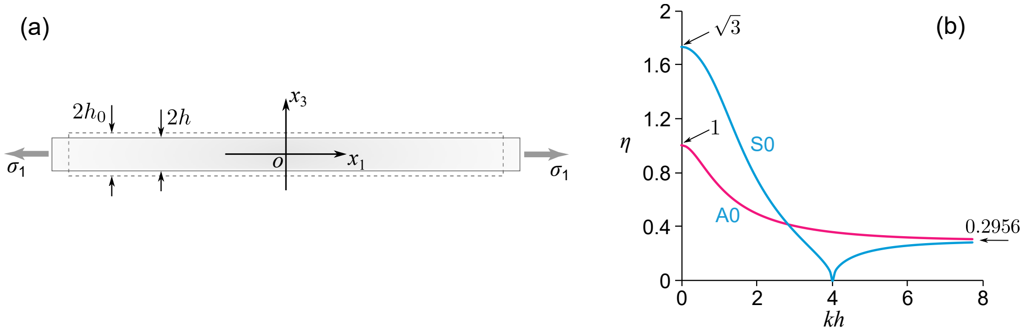

Supplementary Figure 1. (a) Geometry of the stressed film. (b) Master dispersion curves for the fundamental modes, where $\eta_{A0} = \sqrt{(\alpha - \rho v^2)/\gamma}$, $\eta_{S0} = \sqrt{(\rho v^2 - \alpha)/\gamma}$ when $kh \leq 3.99$ and $\eta_{S0} = \sqrt{(\alpha - \rho v^2)/\gamma}$ when $kh \geq 3.99$.

Now we consider the strain energy of isotropic incompressible third-order elasticity,

$$W = \mu\,\mathrm{tr}\boldsymbol{E}^2 + (A/3)\mathrm{tr}\boldsymbol{E}^3, \tag{S.5}$$

where $\boldsymbol{E}$ is the Green-Lagrange strain tensor, μ is the Lamé modulus of linear elasticity ($\mu = E/3$, where E is Young's modulus) and A is the Landau constant of third-order elasticity (also known as n in the expansion of Murnaghan). This strain energy is valid up to moderate strain [4]. It can be checked by hand, or with a Computer Algebra System, that when taking a Taylor expansions for small elongations $\lambda_i - 1$, we obtain the identity[4] $2\beta = \alpha + \gamma$, which substituted into (S.2) leads to

$$s_1^2 = \frac{\alpha - \rho v^2}{\gamma}, \qquad s_2^2 = 1, \tag{S.6}$$

and the dispersion equation takes the compact form (Eq. (1) in the main text),

$$4s_1\left(\frac{\tanh s_1\, kh}{\tanh kh}\right)^{\pm 1} = (1 + s_1^2)^2. \tag{S.7}$$

For the fundamental A0 mode, the speed is always subsonic. We define $\eta_{A0} = \sqrt{(\alpha - \rho v^2)/\gamma}$, and for each value of kh we solve

$$4\eta_{A0} \frac{\tanh \eta_{A0}\, kh}{\tanh kh} = (1 + \eta_{A0}^2)^2, \tag{S.8}$$

numerically for η_{A0}, which leads to the A0 plot on Supplementary Figure 1(b). It starts at $\eta_{A0} = 1$ as $kh \to 0$ and decreases toward 0.2956 (the root of the cubic $x^3 + x^2 + 3x - 1 = 0$) as $kh \to \infty$.

For the S0 modes in the low kh regime, the wave is supersonic and $s_1^2 < 0$. We define $\eta_{S0} = \sqrt{(\rho v^2 - \alpha)/\gamma}$ and for each value of kh we solve

$$4\eta_{S0} \frac{\tanh kh}{\tan \eta_{S0}\, kh} = (1 - \eta_{S0}^2)^2, \tag{S.9}$$

numerically for η_{S0}, which leads to the first branch of the S0 plot on Supplementary Figure 1(b). This equation is valid for $kh \leq 3.9973$ (the root of the equation $4 \tanh x = x$). Finally for $kh \geq 3.9973$, we define η_{S0} as $\eta_{S0} = \sqrt{(\alpha - \rho v^2)/\gamma}$, and we solve

$$4\eta_{S0} \frac{\tanh kh}{\tanh \eta_{S0}\, kh} = (1 + \eta_{S0}^2)^2, \tag{S.10}$$

numerically for η_{S0}, which leads to the second branch of the S0 plot in Supplementary Figure 1(b).

In a material with significant *structural* anisotropy (not only strain-induced anisotropy), potentially due to the presence of aligned collagen or fibers, the propagation and wave speed of the Lamb waves are modified accordingly. In that case the strain energy (S.5) is no longer valid. However, our method could potentially be extended to this scenario, or at least to certain special cases of anisotropy.

SUPPLEMENTARY NOTE 2: SENSITIVITY ANALYSIS

Here we demonstrate how sensitive our prediction is to the stress σ_1 when considering small errors in our measurements. We focus on the sensitively analysis for the anti-symmetric mode A0, as the results for the S0 mode are analogous.

For the analysis, assume for simplicity that for this mode we measure only two wave speeds v_1 and v_2, corresponding to two different wavenumbers k_1 and k_2, respectively. We define $\eta_1 = \sqrt{(\alpha - \rho v_1^2)/\gamma}$ and $\eta_2 = \sqrt{(\alpha - \rho v_2^2)/\gamma}$, which we can solve for α and γ, and substitute into (S.3) to obtain

$$\sigma_1 = \tfrac{1}{2}(\rho v_1^2 + \rho v_2^2) + \tfrac{1}{2}(\rho v_1^2 - \rho v_2^2)F, \qquad \text{where} \qquad F = \frac{\eta_1^2 + \eta_2^2 - 2}{\eta_1^2 - \eta_2^2}. \tag{S.11}$$

There are several potential sources of errors in using this equation to predict the stress, coming from the error in measuring the wave speeds and from the error in estimating the (non-dimensional) wavenumbers $k_1 h$ and $k_2 h$. We investigate the effect of these errors separately.

First we assume there is an error in measuring the wave speeds, which we call $\rho\delta v_1^2$ and $\rho\delta v_2^2$; the resulting error in the stress $\delta\sigma_1$, according to (S.11) is

$$\delta\sigma_1 = \tfrac{1}{2}\rho\delta v_1^2(1+F) + \tfrac{1}{2}\rho\delta v_2^2(1-F), \qquad \text{so that} \qquad \frac{|\delta\sigma_1|}{\rho|\delta v^2|} \le \tfrac{1}{2}|1+F| + \tfrac{1}{2}|1-F|. \tag{S.12}$$

Here we assumed that δv_1 and δv_2 are random and uncorrelated, and used $|\delta v^2|$ to represent the maximum error in the squared velocities. We define $c_1 = \tfrac{1}{2}|1+F| + \tfrac{1}{2}|1-F|$ and plot this quantity in Supplementary Figure 2(c).

Next, we assume the wave speeds have been measured correctly, but that there is an error in estimating the wavenumbers, which leads to

$$\delta\sigma_1 = \tfrac{1}{2}(\rho v_1^2 - \rho v_2^2)\left[\frac{\partial F}{\partial \eta_1}\delta\eta_1 + \frac{\partial F}{\partial \eta_2}\delta\eta_2\right]. \tag{S.13}$$

Then, as we assume the wave speeds were measured accurately, we can use the exact relation $\rho v_1^2 - \rho v_2^2 = \gamma(\eta_2^2 - \eta_1^2)$ to rewrite this equation in the form

$$\delta\sigma_1 = \gamma\frac{\delta\eta_2^2(1-\eta_1^2) - \delta\eta_1^2(1-\eta_2^2)}{\eta_1^2 - \eta_2^2}. \tag{S.14}$$

For third-order elasticity (moderate strains) we have $\gamma \sim \mu$, the initial shear modulus, which we use below. Any error committed when calculating η_1 and η_2 will be a result of an error in evaluating $k_1 h$ and $k_2 h$, as shown by equation (S.8). Hence we can write

$$\delta\eta_1^2 = \frac{\partial \eta_1^2}{\partial(k_1 h)}\delta(k_1 h), \qquad \delta\eta_2^2 = \frac{\partial \eta_2^2}{\partial(k_2 h)}\delta(k_2 h). \tag{S.15}$$

Now there are two ways to commit the errors $\delta(k_1 h)$ and $\delta(k_2 h)$. The first is to miscalculate the frequencies k_1 and k_2, which results in $\delta(k_1 h) = h\delta k_1$ and $\delta(k_2 h) = h\delta k_2$, in which case we can assume the errors are uncorrelated and obtain

$$\frac{|\delta\sigma_1|}{\mu|\delta k|h} \le \left|\frac{\partial \eta_1^2}{\partial(k_1 h)}\right| \frac{|1-\eta_1^2|}{|\eta_1^2 - \eta_2^2|} + \left|\frac{\partial \eta_2^2}{\partial(k_2 h)}\right| \frac{|1-\eta_2^2|}{|\eta_1^2 - \eta_2^2|}. \tag{S.16}$$

Note that $|\sigma_1| < \mu$ for moderate strains, so that the right hand-side is typically smaller than the relative error of the stress. We call c_2 the right hand side of the above inequality and plot it in Supplementary Figure 2(b).

The second way is to miscalculate the film depth h, which results in $\delta(hk_1) = k_1\delta h$ and $\delta(hk_2) = k_2\delta h$, from which we obtain

$$\frac{|\delta\sigma_1|}{\mu|\delta h/h|} \le \frac{1}{|\eta_1^2 - \eta_2^2|}\left|\frac{\partial \eta_1^2}{\partial(k_1 h)}k_1 h(1-\eta_1^2) - \frac{\partial \eta_2^2}{\partial(k_2 h)}k_2 h(1-\eta_2^2)\right|. \tag{S.17}$$

We call c_3 the right hand side of this inequality and plot it in Supplementary Figure 2(a).

To summarise, our expected in error in predicting the stress, denoted by $\delta\sigma_1$, is such that

$$\frac{|\delta\sigma_1|}{\mu} < c_1\frac{|\rho\delta v^2|}{\mu} + c_2|\delta k|h + c_3\frac{|\delta h|}{h}, \tag{S.18}$$

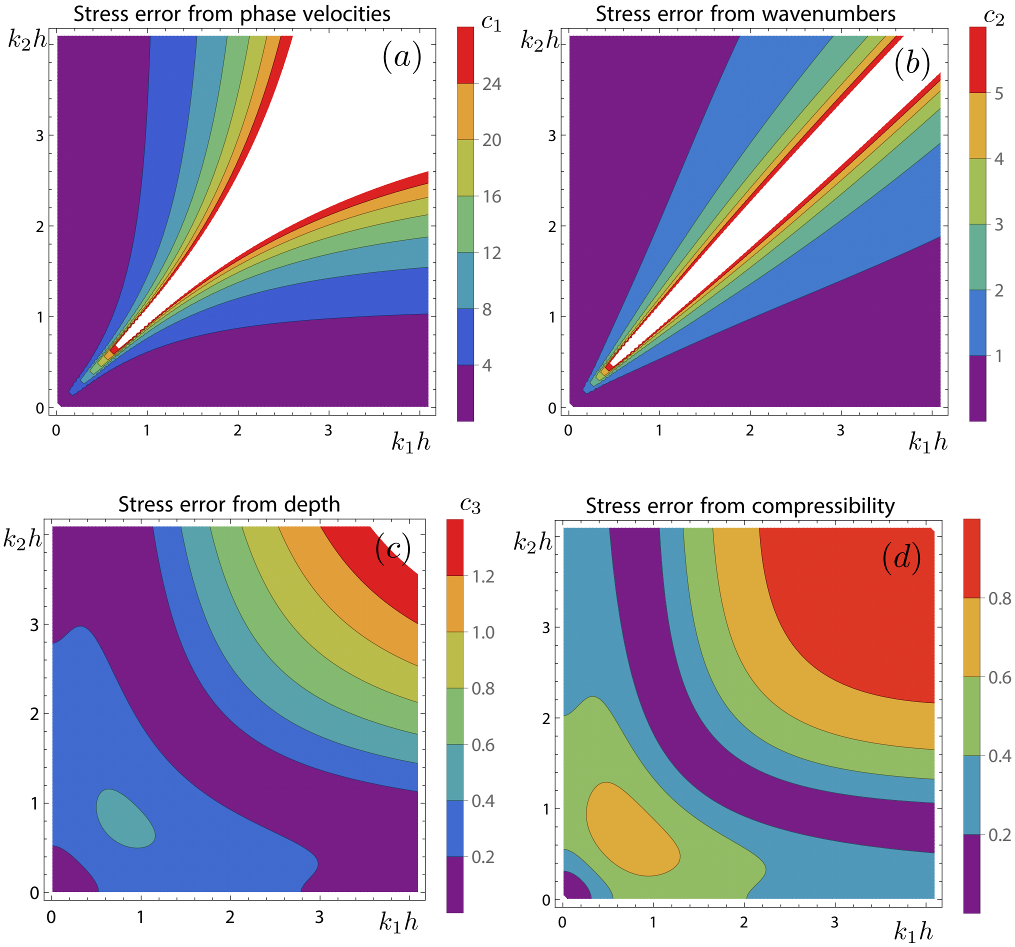

Stress error from phase velocities

Stress error from wavenumbers

Stress error from depth

Stress error from compressibility

Supplementary Figure 2. The graphs show the sensitivity of our prediction of the stress, given by (S.3) due different sources of potential error. In all the figures, it is assumed that the phase speeds v_1 and v_2 of an anti-symmetric Lamb wave are measured at wavenumbers k_1 and k_2, respectively. For every plot, the white regions have errors larger than the values shown in the accompanying legend. Supplementary 2(a) shows how relative errors in the squared speeds v_1^2 and v_2^2 affect the stress. Supplementary Figure 2(b) shows how errors in estimating hk_1 and hk_2 affect the stress prediction. Supplementary Figure 2(c) shows how errors in estimating the depth h magnify, or decrease, the errors in predicting the stress. Finally, the values in Supplementary Figure 2(d) times μ/λ give the error in the stress due to compressibility. For example, if $\mu/\lambda = 1$, and $\mu = 0.02$ GPa, then we would expect an error of 0.016 GPa in the stress when $k_1h = k_2h = 4$.

where δh, δk, δv, are the measurement errors in the sample depth h, the frequency k, and the wave speed v, respectively. The coefficients c_1, c_2, c_3 depend only on the two frequencies used for the measurement, k_1 and k_2, and are independent of the material parameters.

For an example, let us consider the measurements made on the rubber membrane, as shown in Figure 1 of the main paper. Its thickness is $2h \simeq 0.5$ mm. In the case of $N = 0$ (no weights), at frequency $f_1 = 2$ kHz, the speed is $v_1 \simeq 7.5$ m·s^{-1}, so that $k_1h = 2\pi f_1 h/v_1 = 0.42$; at $f_2 = 16$ kHz the speed is $v_2 \simeq 13.4$ m·s^{-1}, so that $k_2h = 1.9$. For these values of k_1h and k_2h we find from Supplementary Figure 2 that $c_2 \sim 0.5$ and $c_3 \sim 0.3$. The wavenumber measurement error of our optical coherence tomography (OCT) system is $\delta k/k \sim 0.1\%$, see Supplementary Note 5. The thickness measurement error $\delta h/h \sim 3\%$ is estimated from the error bars of the thickness, see Supplementary Figure 12 (note that it is because the thickness of the sample is not uniform, not because of the spatial resolution of OCT, which is about 0.018 mm.) Therefore, we expect a prediction error $|\delta\sigma_1|/\mu < 1\%$ (for this calculation, we only included the c_2 and c_3 coefficients, because instead of measuring the speed directly, we calculated it by the formula $v = 2\pi f/k$.)

SUPPLEMENTARY NOTE 3: ALMOST INCOMPRESSIBLE MATERIALS

Our analysis in Section requires that the material be incompressible. Here we show what errors to expect for nearly-incompressible materials.

The equations governing Lamb waves in compressible solids are given by Ogden and Roxburgh [1]. Again, we specialise to third-order elasticity. Then, to take the limit of near-incompressibility, we follow a method used by Shams et al. [4], which in our case leads to taking a series expansion for small μ/λ, where μ and λ are the Lamé constants of linear elasticity. To simplify, and be consistent with third-order elasticity [5], we also consider the strain (or the stress) to be small. The results are

$$\rho v_A^2 = \gamma \eta_A + \alpha + 2(\mu^2/\lambda) F_A(kh), \qquad \rho v_S^2 = \alpha - \gamma \eta_S + 2(\mu^2/\lambda) F_S(kh), \tag{S.19}$$

for the anti-symmetric and symmetric modes, respectively. Here, the terms $F_A(kh)$ and $F_S(kh)$ depend on kh only; for example,

$$F_A(kh) = \frac{(S_2 - 2kh)\eta_A^2(1-\eta_A^2)(1+\eta_A^2)^2}{S(-4C + khS) - 2((5+3C_2)kh - 2S_2)\eta_A^2 + 6S(2C + khS)\eta_A^4 + 4khS^2\eta_A^6 + khS^2\eta_A^8}, \tag{S.20}$$

where $S = \sinh(kh)$, $C = \cosh(kh)$, $S_2 = \sinh(2kh)$, and $C_2 = \cosh(2kh)$. Both F_A and F_S are shown in Supplementary Figure 3.

To investigate the error induced by small compressibility, we use (S.12) together with the above to arrive at

$$\frac{|\delta\sigma_1|}{\mu} = \frac{\mu}{\lambda}\left|F_A(k_1 h)(1+F) + F_A(k_2 h)(1-F)\right|, \tag{S.21}$$

with F given in (S.11).

When the material is only slightly compressible, $\mu/\lambda \ll 1$ and the error is small. However, for more compressible materials, μ/λ is not small; hence for steel [5], $\mu/\lambda \simeq 0.8$. The numerical values of the right hand-side in this equation are shown in Supplementary Figure 2(d).

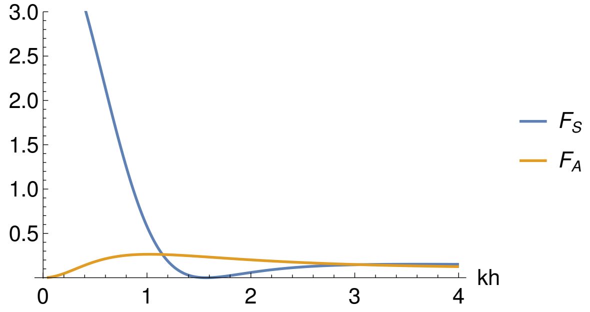

Supplementary Figure 3. Variation of the terms F_A and F_S with kh. When F_S or F_A is small, the Lamb wave speed is insensitive to the material compressibility, and conversely when F_S or F_A is large.

SUPPLEMENTARY NOTE 4: M-B SCAN WITH OPTICAL COHERENCE TOMOGRAPHY TO MEASURE LAMB WAVE PROPAGATION

To study and measure Lamb wave propagation, the OCT system works in a M-B scan mode, which is depicted in Supplementary Figure 4. The laser beam scans synchronously with the stimulus signal sent to the PZT. At each lateral location, we acquire ~ 350 A lines (M scan) at a sampling rate of ~ 43 kHz. Then the laser beam moves to the next localisation (B scan). In total 96 lateral locations are measured. The vibration acquired from each M scan is Fourier-transformed to obtain the amplitude A and phase φ, i.e., $u_3(t) = Ae^{i(\omega t+\varphi)}$. Finally we report the real and imaginary parts of the displacement, $A\cos(\omega t+\varphi)$ and $A\sin(\omega t+\varphi)$, as shown in Figures 5(b) and (d) of the main text.

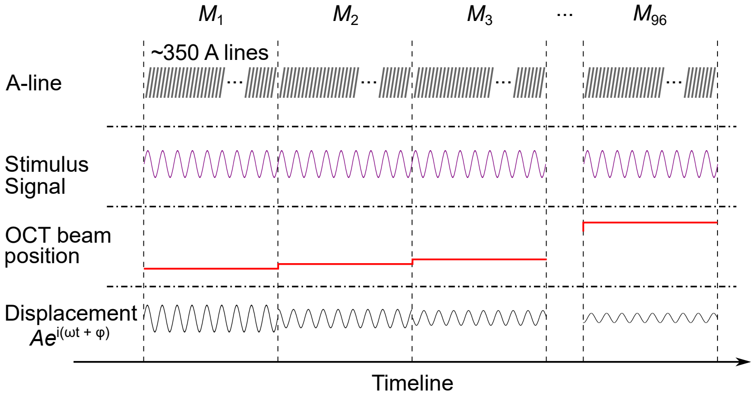

Supplementary Figure 4. Schematic of the M-B scan.

SUPPLEMENTARY NOTE 5: SENSITIVITY IN MEASURING THE WAVENUMBER USING OCT

The standard deviation in the measurement of the vibration amplitude A via a single A-line scan, denoted by δA, is given by the optical signal-to-noise ratio (SNR) [6]: $\delta A = \lambda_0/(4\pi n_0\sqrt{\mathrm{SNR}})$, where λ_0 is the optical wavelength ($\sim$ 1280 nm) and n_0 is the refractive index ($\sim$ 1.4). At the surface of the sample we typically get SNR $\approx$ 40 dB. This sensitivity is improved by a factor $1/\sqrt{M}$ upon averaging of M A-lines. The elastic wave profile is obtained by measuring the displacement at N locations along the propagation direction and then Fourier-transformed to determine its wavenumber k. When the beam scan length covers $\sim$ 3 wavelengths, we find that δk, the standard deviation error of the wavenumber, is given by $\delta k/k \approx \delta A/(A\sqrt{MN})$. With $\Delta A = 20$ nm (see Figure 5(d) of the main text), $M = 350$, and $N = 96$, we obtain $\delta k/k \approx 0.1\%$.

SUPPLEMENTARY NOTE 6: HIGH-ORDER LAMB WAVE MODES EXCITED AT HIGH-FREQUENCY RANGE

When the excitation frequency increases, high-order modes are excited by the probe. Supplementary Figure 5 shows the dispersion relations of the rubber film in the unstressed state. Besides the A0 mode, other wave modes that can be measured from the experiments are also reported. By comparing with the Lamb wave model, it is easy to identify these wave modes as the S0 and A1 modes.

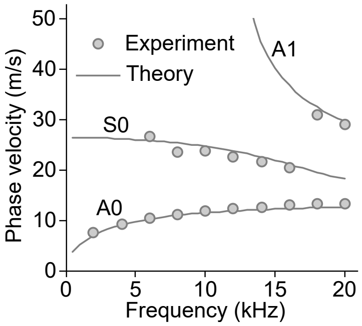

Supplementary Figure 5. Dispersion relations of the different Lamb wave modes (A0, S0 and A1) and comparison with theoretical curves. The theoretical curves are computed using the shear modulus obtained from the tensile test.

SUPPLEMENTARY NOTE 7: MEASURING α AND γ TO DEDUCE THE STRESS AND STRAIN

For the fundamental A0 mode, we have $\rho v^2 = \alpha - \gamma\eta_{A0}^2$. Thus, we simply need to measure v at different frequencies: then for each frequency we have a value of kh, or equivalently, a corresponding value of η_{A0}^2, found by solving (S.8). Then by linear curve fitting we deduce α (the intercept) and γ (the opposite of the slope) and thus σ_1 and λ_1 from (S.3).

Supplementary Figure 6 shows the linear regression when the uni-axial stress is due to $N = 5$ weights, from which we get $\alpha \simeq 314.3$ kPa and $\simeq 147.2$ kPa. According to Eq. (S.3), the stress σ_1 is 167.1 kPa and the stretch λ_1 is 1.29, which agrees well with the applied stress 162.1 kPa and stretch 1.31.

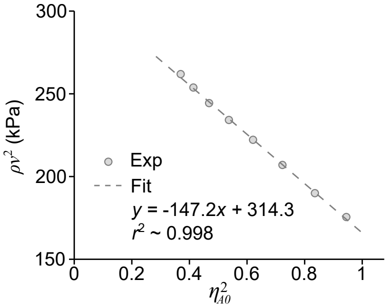

Supplementary Figure 6. Representative curve fitting to identify α and γ. Here $N = 5$ weights added. The linear fitting of ρv^2 to η_{A0}^2 gives $\alpha \simeq 314.3$ kPa and $\gamma \simeq 147.2$ kPa ($r^2 = 0.998$).

SUPPLEMENTARY NOTE 8: LAMB WAVES TRAVELING PERPENDICULAR TO THE UNIAXIAL STRESS

The analysis for the Lamb wave traveling along x_2 (see Supplementary Figure 7) is the same as that for the wave along x_1. It yields the elastic moduli α' and γ', say, which give

$$\alpha' - \gamma' = \sigma_2, \qquad \alpha'/\gamma' = \lambda_2^2/\lambda_3^2. \tag{S.22}$$

For a general biaxial stress state, we solve Eqs. (S.3) and (S.22) to get the stretch ratios λ_1 and λ_2 (recalling that $\lambda_1\lambda_2\lambda_3 = 1$). In our experiments, the rubber film was uni-axially stretched ($\lambda_2 = \lambda_3 = \lambda_1^{-1/2}$), and we expect $\alpha' = \gamma'$ and $\sigma_2 = 0$.

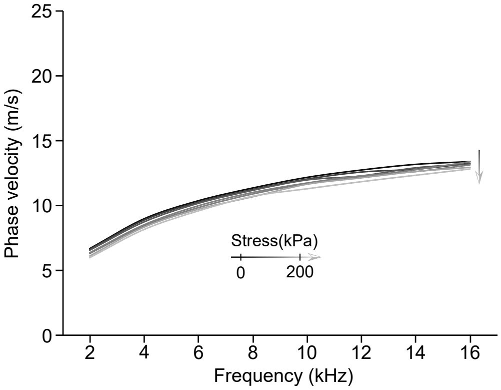

Supplementary Figure 7. Dispersion relations of the Lamb waves traveling perpendicular to the uniaxial stress. The phase velocities decrease when the stress increases. Here we find that $|\sigma_2| < 4$ kPa, which is indeed almost zero compared to σ_1.

SUPPLEMENTARY NOTE 9: TENSILE TEST OF THE RUBBER FILM

Supplementary Figure 8 shows the tensile test and the fitting curve. The infinitesimal shear modulus $\mu \simeq 180$ kPa is obtained by fitting the initial stage (stretch ratio < 1.07) of the stretch-stress curve. To fit the whole curve we use the Mooney-Rivlin model $W = C_{10}(\lambda_1^2 + \lambda_2^2 + \lambda_3^2 - 3) + C_{01}(\lambda_1^2\lambda_2^2 + \lambda_2^2\lambda_3^2 + \lambda_3^2\lambda_1^2 - 3)$, with $C_{10} \simeq 51$ kPa and $C_{01} \simeq 39$ kPa. Then we recall that the Mooney-Rivlin model is equivalent, at the same level of approximation, to the general model of third-order elasticity (S.5), with the connections [7] $\mu = 2(C_{10} + C_{01})$ and $A = -8(C_{10} + 2C_{01})$, or here, $\mu = 180$ kPa, $A = -1,302$ kPa.

These material parameters are used in the main text to produce theoretical dispersion curves and confirm the match with the experimental data, although ultimately they are not needed for our stress measurement method through OCT imaging.

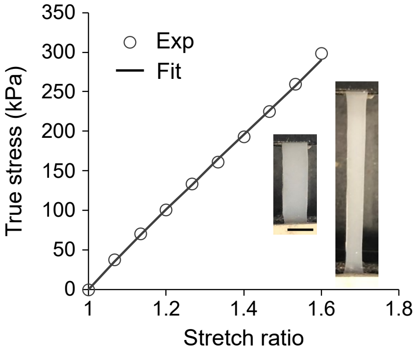

Supplementary Figure 8. Tensile test of the rubber film. Inset, photos of the undeformed and deformed sample. Scale bar, 5 mm.

SUPPLEMENTARY NOTE 10: CHARACTERISATION OF THE *BODHRÁN*

To show that the tension can be reduced by wetting the inner side of the *bodhrán* skin, and so that the vibration frequencies change, we used the experimental setup depicted in Supplementary Figure 9(a) to characterize the fundamental vibration frequencies of the dry and wet bodhrán. The *bodhrán* was beaten at its center every 10 seconds and then the sound was measured with a cellphone using the Google Science Journal App. The cellphone was placed about 10 cm away from the skin. As shown in Supplementary Figure 9(b), the fundamental vibration frequency was ~ 84 Hz in the dry state. However, wetting the skin, as shown in Supplementary Figure 9(c), decreases the vibration frequency to ~ 36 Hz.

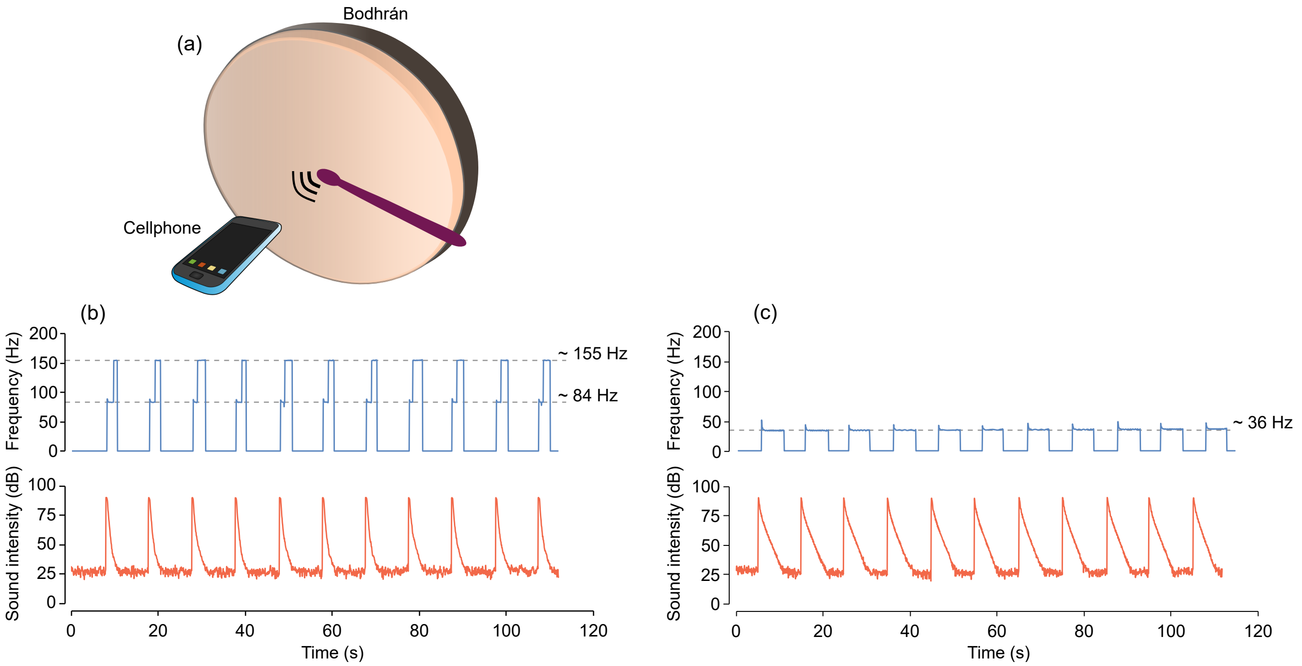

Supplementary Figure 9. Vibration frequency of the *bodhrán*. (a) Schematic of the experiment. The *bodhrán* is beaten every 10 seconds and then the sound intensity and frequency are measured by a cellphone. (b) Dry state. The fundamental and second harmonic frequencies can be measured: ~ 84 Hz and ~ 155 Hz. (c) Wet state. The fundamental frequency drops to ~ 36 Hz.

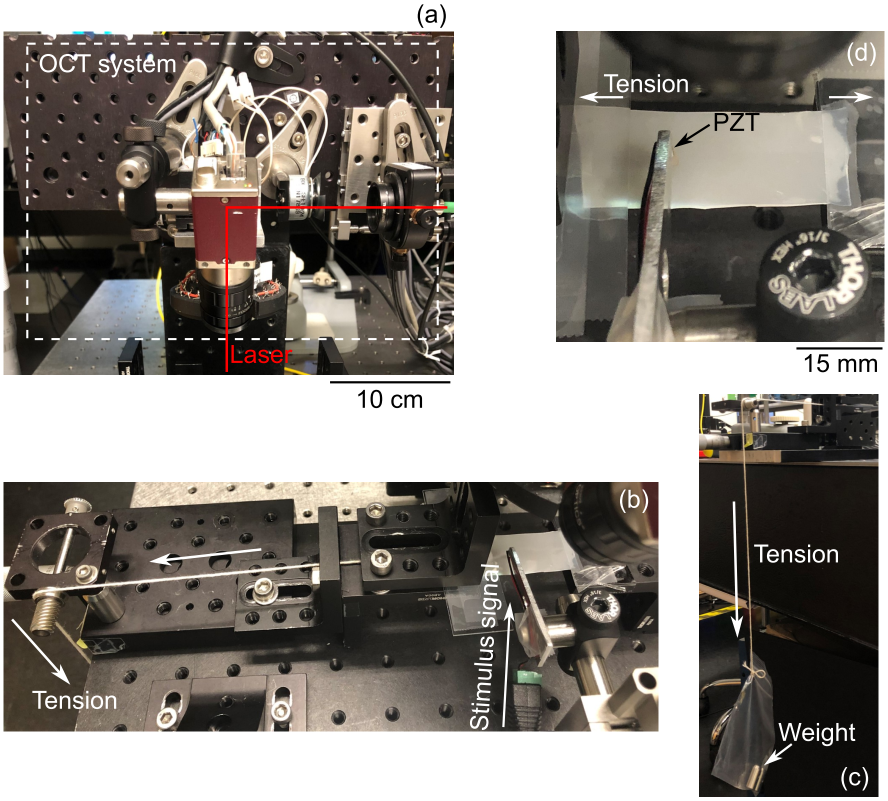

Supplementary Figure 10. Photos of the experimental setup. (a) Scanning laser of the OCT system. (b) and (c) show how stress is applied to the film by a simple pulley/weight apparatus. (d) A zoomed-in view of (b) showing the sample and the PZT that is used to drive the vibration of the probe.

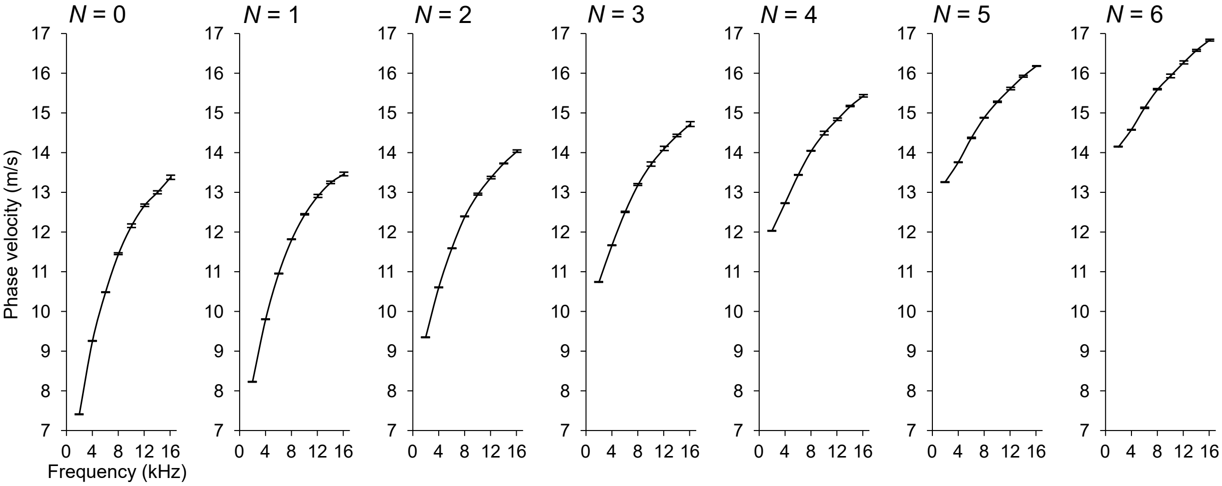

Supplementary Figure 11. Standard deviations of the experimental data shown in Figure 1(f) of the main text. Here, N indicates the number of the weights.

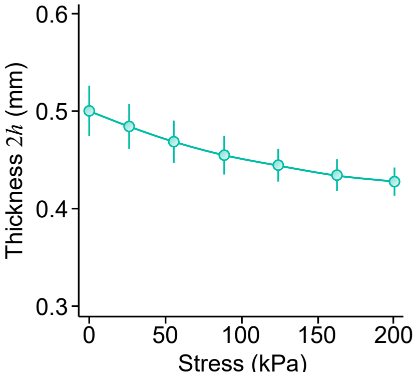

Supplementary Figure 12. Variation of the rubber sheet thickness (as tracked by OCT) with the stress, from $N = 0$ (stress-free) to $N = 6$ weights of 20 g each. As expected, the thickness decreases as we increase the stress, due to the Poisson effect. Error bars indicate standard deviations over five measurements performed at different locations of the sample.

SUPPLEMENTARY REFERENCES

---

[1] Ogden, R. W. & Roxburgh, D. The effect of pre-stress on the vibration and stability of elastic plates. *International Journal of Engineering Science* **31**, 1611–1639 (1993).

[2] Shams, M., Destrade, M. & Ogden, R. W. Initial stresses in elastic solids: Constitutive laws and acoustoelasticity. *Wave Motion* **48**, 552–567 (2011).

[3] Gower, A. L., Shearer, T. & Ciarletta, P. A new restriction for initially stressed elastic solids. *Quarterly Journal of Mechanics and Applied Mathematics* **70**, 455–478 (2017).

[4] Destrade, M., Gilchrist, M. D. & Saccomandi, G. Third-and fourth-order constants of incompressible soft solids and the acousto-elastic effect. *Journal of the Acoustical Society of America* **127**, 2759–2763 (2010).

[5] Li, G.-Y., Gower, A. L. & Destrade, M. An ultrasonic method to measure stress without calibration: The angled shear wave method. *Journal of the Acoustical Society of America* **148**, 3963–3970 (2020).

[6] Ramier, A., Cheng, J. T., Ravicz, M. E., Rosowski, J. J. & Yun, S.-H. Mapping the phase and amplitude of ossicular chain motion using sound-synchronous optical coherence vibrography. *Biomedical Optics Express* **9**, 5489–5502 (2018).

[7] Destrade, M., Gilchrist, M. D., Murphy, J.G. Onset of nonlinearity in the elastic bending of blocks. *Journal of Applied Mechanics* **77**, 061015 (2010).